The ultra-fast oxidation rate of a synthetic Fe-based oxygen carrier: experiment and simulation study

Zirui He [a,b,*], Florent Minette [a,b], Juray De Wilde [a,b,*]

[a] Université catholique de Louvain, Institute of Mechanics, Materials and Civil Engineering (iMMC) Materials & Process Engineering (IMAP), Place Sainte Barbe 2, B-1348 Louvain-la-Neuve, Belgium

[b] Research and Innovation Centre for Process Engineering (ReCIPE), Place Sainte Barbe 2, B-1348 Louvain-la-Neuve, Belgium

Abstract The knowledge of the oxidation rate of the oxygen carrier (OC) is essential in designing and optimizing chemical looping processes. However, the oxidation is usually too rapid that the measured rate by TGA deviates from the intrinsic ones because of the transport limitations. In this work, a micro-fixed bed reactor was employed to investigate the oxidation rate of a synthetic Fe-based oxygen carrier (OC) via temperature-programmed oxidation, and step response experiments carried out at 300-450°C to lower the oxidation rate as much as possible. The synthetic Fe-based OC showed a very fast initial stage that consumed all the feed O_2, and temperature-dependent Fe conversion after the initial stage. The experimental results were analyzed by simulations using a 1D heterogeneous reactor model accounting for potential interfacial mass transfer limitations. Even at a temperature as low as 300°C, O_2 was fully consumed in the initial stage, so that only minimum oxidation rates could be estimated. The estimated minimum oxidation rate is, however, faster than those reported in the literature, and indicates that Fe in the OC is fully converted within 3s with 2% O_2 at 450°C. The fast oxidation rate leads to a sharp reaction front propagating in the reactor at 450°C. Based on the estimated minimum oxidation rate, we suggest using the rate equation $r_{O2}=883*exp(-32000/RT)*(1-x_s)^{2/3}C^s_{O2}$ to estimate the magnitude of oxidation rate of the Fe-based OC at higher temperature. This estimation indicates that the oxidation rate is faster than the typical mass transfer rate in a bubbling fluidized bed, and similar to that in a riser.

Keywords: Chemical Looping; Oxygen carrier; Oxidation; Kinetics modeling

* Corresponding authors: Zirui He: zirui.he@uclouvain.be, Juray De Wilde: juray.dewilde@uclouvain.be, Tel: +32 10 47 81 93

1 Introduction

Chemical looping (CL) processes are promising for not only CO_2 capture, but also emission reduction, energy conservation, and value-creation [1–3]. Chemical looping combustion and reforming are the most widely studied chemical looping processes in the past decades, which contain at least two steps where the oxygen carrier (OC) respectively reacts with O_2 (in air reactor, AR) and fuel (in fuel reactor, FR) [3,4].

The knowledge of reaction kinetics of OCs is of great importance in modeling and designing the CL processes, especially for scaling-up and their optimization. The thermogravimetric analyzer (TGA) has been widely used to determine the reaction kinetics as it gives the weight loss/gain of the OC during reduction/oxidation (RedOx) reactions, seemingly simple for interpretation [5–7]. However, because the gaseous reactant and product have to diffuse through the stagnant gas in the sample container (usually a crucible), the fast reactions suffer from significant diffusion-resistance from the bulk gas to the crucible in TGA [8–11]. Kinetics modeling of the TGA experiments considering the bulk gas concentration results in significant error in both activation energy and reaction order [9]. In addition, the flow pattern in the TGA and the dimension of the used crucible differ one from another, making the lack of consensus in the measured kinetics, especially for fast ones [12]. Micro-fluidized bed (MFB) has been used to study the RedOx kinetic of the OCs as it provides better heat and mass transfer than that in TGA [13–17]. Li et al. [18–20] further reported a combination of MFB and TGA for measuring the RedOx kinetics of different kinds of OC and found a 4 times faster rate in the MFB-TGA reactor compared to that measured in traditional TGA. The interpretation of the MFB experiments relays on either a well-mixed assumption for particles (and may be also for gas), or the simulation of the fluidized bed using the two-phase model in which a number of correlations have to be used, e.g., correlations for bubble diameter, interexchange coefficient, and interfacial mass transfer coefficient [21,22]. In addition, the prevailed wall effect in micro fluidized bed results in complicated hydrodynamic phenomena [23]. Thus, more uncertainties were brought into the kinetics analysis. Typically, low conversion of gaseous reactant is required for the experiments performed in MFB to allow using the mean concentration of gaseous reactant in the reactor for kinetics modeling [13,20]. The low gaseous reactant conversion requires high bed dilution for fast reactions, whereas the main transport limitation in the fluidized bed is bubble-emulsion mass transfer. As a result, the gas concentration in emulsion phase (gas around the reactive particles) can be very different from the mean concentration even with a low observed conversion of gaseous reactant [24], which results in error during kinetic modeling.

Because Fe-based materials are cheap and environmentally friendly, they have been widely studied as the OC for CL processes [25–29]. However, as a very active metal, the oxidation of Fe-based OC is

very fast. Abad et al. [5,30,31] studied the oxidation of both synthetic and naturally existed materials and observed very high oxidation rate and negligible influence of temperature on oxidation. Considering the inherent mass transfer resistance in the TGA experiments, the weak influence of temperature on reaction rate should be verified by other experimental technique. On the other hand, fast oxidation rate causes high thermal output as oxidation of Fe is highly exothermic, which causes hot spot and agglomeration with inappropriate reactor. Hu et al. [32] performed the cyclic oxidation and reduction of $MgAl_2O_4$-supported OC with different Fe_2O_3 content in fluidized bed. They found the OC containing 30%, 40%, and 50% Fe_2O_3 suffered from severe deactivation and defluidization during RedOx cycles, which is attributed to the hot spot during oxidation. The oxidation rate should be well-understood to allow selecting appropriate reactor. Li et al. [19] found that, when designing a AR with the observed oxidation rate in the novel MFB-TGA reactor, the AR should be operated in dilute transport region for short residence time. These two examples emphasis the importance of studying the oxidation in well-defined conditions to evaluate the oxidation rate. The micro-fixed bed reactor is a "simpler" reactor in terms of the flow pattern, and the well-defined reaction conditions can be achieved to facilitate the data interpretation. For example, the bypass of gaseous reactant, e.g., bulk flow in TGA and bubble phase in fluidized bed reactor, is negligible in micro-fixed bed reactor if the bed dilution is in the acceptable range. It is also possible to exclude the external heat and mass transfer limitations [33], thus, the micro-fixed bed reactor has been widely used in studying the fast reaction kinetics [34–38].

In this work, a Fe-based, $MgAl_2O_4$ supported oxygen carrier is designed and synthesized. The oxidation of the OC by O_2 was performed in a micro-fixed bed reactor to allow better evaluating the oxidation rate. The oxidation rate is estimated by modeling the micro-fixed bed reactor with 1-D heterogeneous fixed bed model. This work gives a fresh view of the ultra-fast oxidation rate of the Fe-based OC.

2 Experimental

2.1 Prepare the oxygen carrier

$MgAl_2O_4$ is used as the inert support of OC because it has a very high melting point and hardly reacts with the active metals [39–41]. The OC was prepared using the wet impregnation. The porous $MgAl_2O_4$ (Puralox MG28, Sasol Germany GmbH) was dried at 120°C before impregnation. $Fe(NO_3)_3{\cdot}9H_2O$ was dissolved into denoised water with continuous stirring using a magnetic stirrer. $MgAl_2O_4$ particle was added into the solution to have 20% Fe_2O_3 on $MgAl_2O_4$ after calcination. The slurry was then stirred at 80°C to evaporate part of the water in the solution. When it was dense, the slurry was dried at 150°C.

The obtained sample was calcined in a muffle furnace at 900°C for 2h. Then the particle was pelletized, crushed, and sieved for the desired size range, 150-200µm.

2.2 Experimental setup and procedure

The setup used to study the oxidation of the OC is schematically shown in Figure 1. Two kinds of test, cyclic oxidation/reduction test and temperature programmed oxidation (TPO) were performed, while the reduction is not presented here. The cyclic test was performed by oxidizing with O_2/Ar mixture and reducing with H_2/Ar mixture. The flow rate of Argon, 20% O_2 in Argon, and hydron were regulated using mass flow controllers (MFC, EF-L from Bronkhorst, and SLA5850 from Brooks). A 4-way pneumatically actuated valve was used to switch between the reducing gas, H_2/Ar mixture, and the oxidation gas O_2/Ar mixture. At both the inlet and the outlet of the reactor, two pressure transmitters were used to monitor the pressure drop, while the pressure at the exit of the 4-way valve to the vent was monitored and adjusted with a metering valve to be the same pressure as the inlet of the reactor to reduce the fluctuation during gas switching. The reactor is made from a 12×10mm Inconel 625 tube. The OC was diluted with α-alumina particles (dilution ratio ~ 1:5) and then loaded into the reactor. The packed bed consists of a bottom porous alumina plat (2 mm) with 100 µm pore size. A layer of alumina was put on the plat, upon which was the mixture of alumina and the oxygen carrier. On the top of the reactive bed, about 5 mm of alumina particle was loaded acting as gas distributor and preheater. Empty bed test with was performed with only alumina particles and verified the negligible effect of the RedOx of the tube and the adsorption of reactant by porous alumina. The effluent gas was continuously analyzed by the mass spectrometer (QGA, Hiden analytic) and the gas sample was taken directly from the exit of the reactor to have the best transit measurement. H_2, Ar, and O_2 are measured at m/z = 2, 20, and 32 respectively. Using m/z=20 to measure Argon allows having similar peak density of Ar and other gas to increase the measuring frequency. During oxidation, O_2 and Ar were measured while during reduction, H_2, H_2O, and Ar were measured. The mass spectrometer was calibrated before each reduction or oxidation test to ensure stability and accuracy.

The TPO was performed with fresh OC. Firstly, the OC was reduced at 800°C. Then the reactor cooled down while being pressurized to 3bar with a continuous flow of Ar. After the reactor cooled down to room temperature, the pressure was reduced to ambient pressure, and the gas was switched to 100 Nml/min 2% O_2 in Ar. Then the furnace was heated up with 4.5°C/min ramping. The gas at the exit of the reactor was continuously measured.

At the beginning of the cyclic oxidation/reduction experiments, the reactor was heated up under Ar (from oxidation stream) flow with 10°C/min ramping. During this time, the MS was stabilized using the desired O_2/Ar mixture. After stabilizing, the MS was calibrated with 20% O_2 in Ar and then switched

back to measure the desired reacting steam for at least 5 min to ensure stability. When the MS was certainly stabilized, the MS was connected to the exit of the reactor to measure the gas from the reactor, which was pure Argon at this time. After reaching the desired temperature, the Ar flow rates of both reduction and oxidation were increased to the same flow rate, 600 ml/min. The metering valve on the 4-way valve venting line was adjusted to have the same outlet pressure in both lines. When the pressure was stabilized, the gas was switched to reacting gas. The MS usually observed an O_2-free period, then a gradual increase of the concentration of the reactant. After the gas concentration became the same as feeding gas for about 1 min, the gas was switched to Ar again to purge the reactor for 2 min. The O_2/Ar mixture was switched back again to verify if the reaction was actually finished and to verify the step response. Usually, this second step took 2 min and was followed by the purging of the reactor using Ar. The oxidation/reduction test was repeated more than 40 times and no deactivation was observed. The experimental conditions are summarized in Table 1. The oxygen uptake is calculated by trapezoidal integration:

$$\mathrm{U}_{\mathrm{O}_2} = \sum_{T^1}^{T^i} F_{tot} \cdot 0.5 \cdot \left(\delta yO_2^i + \delta yO_2^{i-1}\right) \cdot \left(T^i - T^{i-1}\right) \quad (1)$$

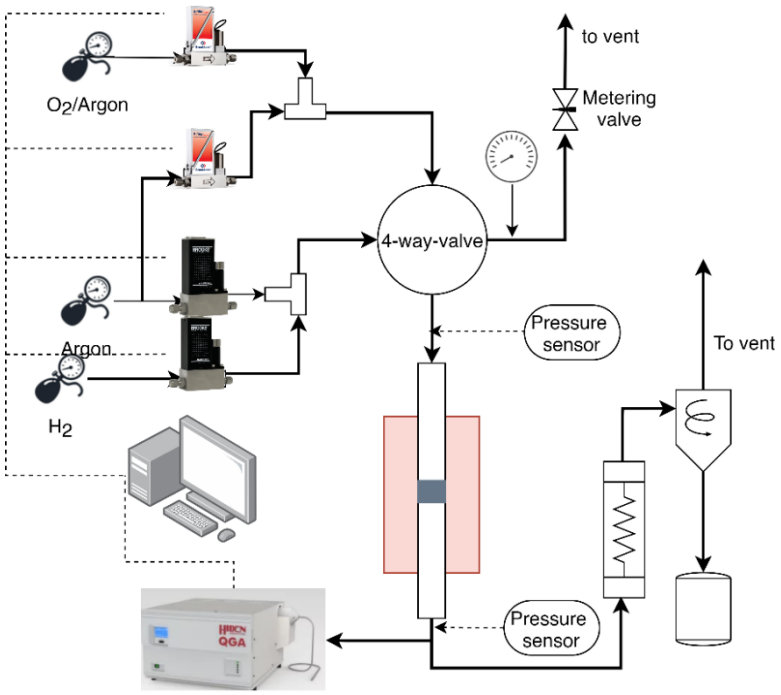

Figure 1. Schematic of the setup for the kinetic test.

Table 1. Experimental conditions.

Reactor diameter	0.01 m
Total flow rate	600 Nml/min
Temperature	300 – 450°C
O_2 concentration	1-20%

2.3 Microstructure

The microstructure of the OC is characterized using SEM. Figure 2 shows the SEM images of the Sasol-$MgAl_2O_4$ and the oxygen carrier with 20% Fe_2O_3. It is seen that the inert support particles are porous spheres with 10-30µm diameter. The right figure shows the impregnated Fe_2O_3 exists like fine filaments on the inert support that may favor gas-solid reactions.

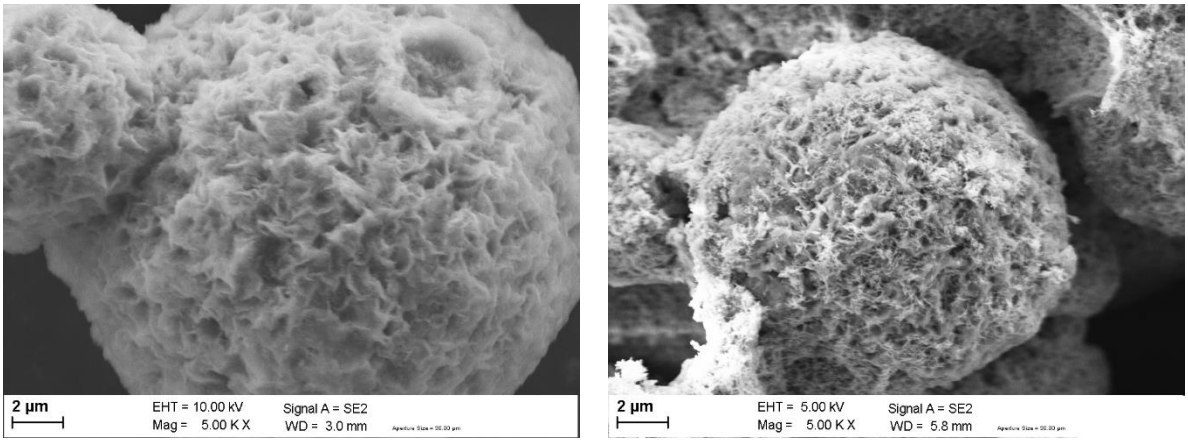

Figure 2. SEM image of the (left) inert support ($MgAl_2O_4$) and (right) 20% Fe_2O_3 on $MgAl_2O_4$.

3 Modeling the oxidation experiment

3.1 The heterogeneous fixed bed model

The reactor is modeled with a 1-D heterogeneous fixed bed model with axial dispersion, considering the gas-solid mass and heat transfer [42], as schematically shown in Figure 3. Usually, the experiment in a micro-fixed bed reactor should guarantee negligible axial dispersion by imposing high superficial gas velocity. However, in this work, this is limited by pressure drop (with 600Nml/min the pressure drop in the reactor is about 0.15 bar at 450°C). Thus, the axial dispersion term is considered. The continuity and energy equations of the bulk gas phase are:

$$\varepsilon_g \frac{\partial C_A}{\partial t} = -u_{sg} \frac{\partial C_A}{\partial z} + \left(\varepsilon_g D_A \frac{\partial^2 C_A}{\partial z^2} \right) - k_g a_v \varepsilon_{as} \left(C_A - C_{A,s}^s \right) \quad (2)$$

$$\varepsilon_g \rho_g C_p \frac{\partial T}{\partial t} = -u_s \rho_g C_p \frac{\partial T}{\partial z} - h_f a_v \varepsilon_s (T - T_s^s) \quad (3)$$

where C_A and C^s_{As} are respectively the gas concentration in bulk gas and on solids surface, [mol/m^3_g], ε_g is the void fraction of gas in the micro-fixed bed, [m^3_g/m^3_r], u_{sg} is the superficial gas velocity, [$m^3_g/m^2_r \cdot s$], D_A is the diffusivity of reactant A, k_g is the interfacial mass transfer coefficient, [$m^3_g/m^2_p \cdot s$], $a_v=6/d_p$ is the specific surface area of particles, [m^2_s/m^3_s], ε_{as} is the fraction of active solids, [m^3_{as}/m^3_r], T and T^s_s are the gas and solids surface temperature,[K], ρ_g is the density of gas, [kg/m^3_g], C_p is the specific heat capacity, [$kJ/kg \cdot K$], h_f is heat transfer coefficient around particles, [$kJ/m^2_s \cdot s$].

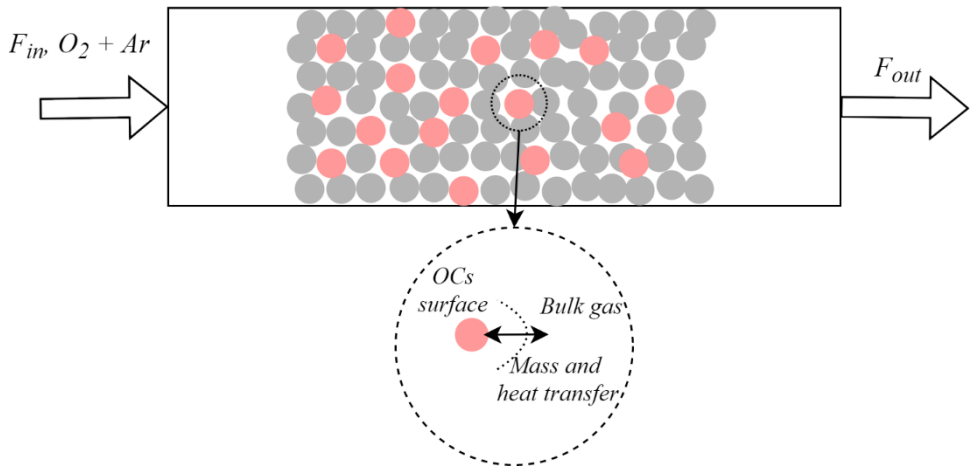

165

166 *Figure 3. Schematic of 1D heterogeneous fixed model.*

167 The boundary conditions are:

168 at z = 0

169 $$u_{sg}C_A = \left(\varepsilon_g D_A \frac{\partial C_A}{\partial z}\right) + F_A^{in} \quad (4)$$

170 $$T = T_0 \quad (5)$$

171 at z = L

172 $$\frac{\partial C_A}{\partial z} = 0 \quad (6)$$

173 The continuity equation of gaseous species on the active particles is:

174 $$\varepsilon_{as}\epsilon_g \frac{\partial C_{As}^s}{\partial t} = \varepsilon_{as} k_g a_v (C_A - C_{As}^s) - \rho_{as} r_A (C_{As}^s, T_s) \quad (7)$$

175 where ϵ_g is the voidage fraction of the particles. The continuity and energy equations of solid phase
176 are:

177 $$\frac{\partial C_s}{\partial t} = -r_s \quad (8)$$

178 $$(1-\varepsilon_g)\rho_s C_{p,s} \frac{dT_s^s}{dt} = h_f a_v (1-\varepsilon_g)(T - T_s^s) - \Delta H \rho_{as} r_A \quad (9)$$

179 where C_s is the concentration of solids reactant, [*mol/kg*^{s}]. The mass transfer coefficient between
180 the bulk gas and solids is calculated as following [42]:

181 $$k_g = \frac{j_D G}{M_m y_{fA}} Sc^{-\frac{2}{3}} \quad (10)$$

$$j_D = \begin{cases} 1.66(Re)^{-0.51}, & Re = \dfrac{d_p G}{\mu} < 190 \\ 0.983(Re)^{-0.41}, & Re = \dfrac{d_p G}{\mu} > 190 \end{cases} \quad (11)$$

$$y_{fA} = \frac{(1+\delta_A y_A) - (1+\delta_A y_A^S)}{\ln\left(\dfrac{1+\delta_A y_A}{1+\delta_A y_A^S}\right)} \quad (12)$$

$$M_m = \sum y_j M_j \quad (13)$$

$$Sc = \frac{\mu_m}{\rho_m D_{AB}} \quad (14)$$

where δ_A is the expansion factor that is -1 for oxidation of Fe by O_2. The diffusivity of A in B, D_{AB}, is calculated by the semiempirical relation of Fuller-Schettler-Giddings [43]:

$$D_{AB} = \frac{10^{-3} T^{1.75} \left(\dfrac{1}{M_A} + \dfrac{1}{M_B}\right)^{0.5}}{p_t \left[(\sum v_A)^{\frac{1}{3}} + (\sum v_B)^{\frac{1}{3}}\right]^2} \quad (15)$$

$$\mu_m = \sum y_j \mu_j \quad (16)$$

where M_A and M_B are in [*g/mol*], p_t is pressure in atm, temperature is in K.

3.2 Modeling the oxidation reaction

The 1-D heterogeneous fixed bed model requires a particle scale model to calculate the reaction rate, $r_A(C_{As}^S, T_s)$. In this work, an empirical gas-solid reaction model is used and the reaction rate is postulated to be first order with respect to O_2:

$$r_{O_2} = k_r (1 - x_s)^n C_{O_2,s}^S \quad (17)$$

With *n* equal to 1, 2/3, 0.5 and 0, the model represents homogeneous model (F1), tri-dimensional shape and bi-dimensional shape contracting phase-boundary controlled reaction, and zero-order model, respectively. In the first step, *n* and k_r were fitted as parameters. Then model with the closest *n* as the best fit of *n* is used to simulate the reactor. The oxidation is one-step process, as indicated by Grosvenor et al. [44,45]:

$$\frac{4}{3}\mathrm{Fe} + \mathrm{O_2} \rightarrow \frac{2}{3}\mathrm{Fe_2O_3}, \qquad \Delta H_r^0 = -549.5\ [kJ \cdot mol^{-1}] \quad (18)$$

It is noted that the stiffness of the PDEs coupling flow and reaction is significant due to the fast reaction. In addition, the reaction suddenly stops when all the Fe is oxidized leads to numerical

instability, especially when *n<1*. These two features of the PDE set make solving the equation set a hard task. To ease the instability, the F2 model is used in the ending period of the oxidation with:

$$r_{O_2} = \varphi_{ox} k_r C_{As}^{s} (1 - x_s)^2, \qquad \text{for } (x_s > 0.95) \tag{19}$$

where $\varphi_{ox} = 0.05^n / 0.05^2$. This treatment didn't change the results in the simulation before x_s reaches 0.95 while keeping the continuity of the oxidation rate.

3.3 Objective function and software

The objective function below is considered:

$$f_{obj}(k_r, n) = \sum \left(y_{O_2}^{i,exp.} - y_{O_2}^{i,sim.}(k_r, n) \right)^2 \tag{20}$$

where $y_{O_2}^{i,exp.}$ is the O_2 exit concentration at i^{th} time during the oxidation experiment while $y_{O_2}^{i,sim.}(k_r, n)$ is the exit O_2 concentration at i^{th} time with parameter k_r and n.

To solve this PDE equation set, a spatial grid size similar to the particle size was used to allow simulating the very rapid gas-solid reaction. The first-order upwind differencing scheme was used for the convection term, while the second-order centered differencing scheme was used for the diffusion term. Julia programing language [46] was used because of its complete ecosystem of ODE solvers, and the package DifferentialEquations.jl [47] was to solve this problem. The KenCarp47 solver, an A-L stable stiffly-accurate 4th order seven-stage ESDIRK method with splitting, was used for time integration [48].

4 Results

4.1 Temperature programmed oxidation

Firstly, the TPO test was performed with 2% O_2 in Argon and the result is shown in Figure 4. The detectable consumption of O_2 started below 100°C. The consumption of O_2 increased with temperature and there are two O_2 consuming peaks at ~275°C and 430°C respectively. Actually, the oxidation of Fe by O_2 was found to occur at room temperature and the product is Fe_2O_3, but the growth of the product layer is limited at low temperature that limits the conversion of Fe [45]. In addition, Grosvenor et al. [44] found the thin film of Fe-oxide formed after short oxygen exposure time consisted of Magnetite and Maghemite, indicating the cationic diffusion in the product layer. Hence, the oxidation of Fe by O_2 is one-step to Fe_2O_3, while the dual-peaked curve is the result of the activation of cationic diffusion in the grains. Buelens et al. [49] used in-situ XRD to study the oxidation of Fe by CO_2 and found the metallic Fe was oxidized one step to Fe_3O_4 while the reaction started being detectable around 300°C. Generally speaking, it is much easier that Fe being oxidized by O_2 than that

by CO_2. Thus, further oxidation experiments were carried out 300-450°C to lower the oxidation rate as much as possible. Although the experimental temperature was very low compared with the typical temperature in chemical looping processes practices, it did represent the oxidation of Fe because the two peaks of consuming O_2 are around 275°C and 430°C.

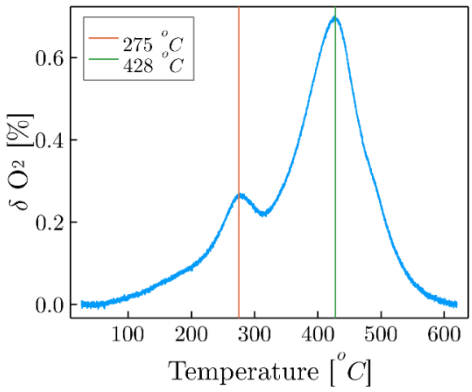

Figure 4. O_2 concentration difference during TPO with 2% O_2 with 5°C/min ramping.

4.2 Influence of temperature on the observed oxidation rate

Oxidation was tested at different temperatures with 0.75g of OC (blended with Al_2O_3 for ~4g bed material) with various oxygen concentrations. The exit O_2 concentration was the only measured parameter during the oxidation experiments and it represent the observed oxidation rate. Figure 5 shows the O_2 breakthrough curve and O_2 uptake in [*mmol*] for the experiments with 1% O_2 in Ar at 300-450°C. It is seen that the exit O_2 concentration was always zero during the initial reaction period, even at a temperature as low as 300°C that is much lower than the temperature in the chemical looping practices. As O_2 was fully consumed for every temperature, the observed initial oxidation rates were the same that was limited by the supply of O_2. The flow rate of reacting gas can, however, not be increased as the pressure drop became unacceptable at higher flow rate. Reducing the OC loading in the reactor will be discussed later.

After a certain time, the O_2 concentration increased, and the time required to detect a significant concentration of O_2 increased with temperature. Further increase of oxidation temperature upon 450°C did not increase O_2 uptake. The maximum O_2 uptake of 0.75g OC was ~1.14 mmol at a temperature higher than 450°C, indicating that the OC contains ~16% active Fe_2O_3.As O_2 was consumed exclusively for the oxidation of O_2, the Fe conversion after the initial fast period was temperature-dependent. At lower temperature, the oxidation conversion increased slowly after the initial fast stage, which is explained by the fact that the oxidation of OC includes a kinetic-controlled fast stage and a slower diffusion-controlled stage [50]. Actually, Grosvenor et al. found that the Fe_2O_3 product layer was formed almost instantly on pure Fe even at room temperature and the oxide layer was thicker at

higher temperatures while the thickness of the oxidation layer increased very slowly, indicating the oxidation conversion after kinetic-controlled stage was also temperature dependent between 25-150°C [44,45]. Thus, the temperature-dependent Fe-conversion is explained by different product layer thickness formed at different temperature. The temperature-dependent conversion was also observed in the oxidation of Nickel foil at 800-1000°C. Zhao et al. [51] observed an O_2 free period during oxidation of Ni foil and the Ni conversion was slightly higher at a higher temperature after the initial O_2-free period.

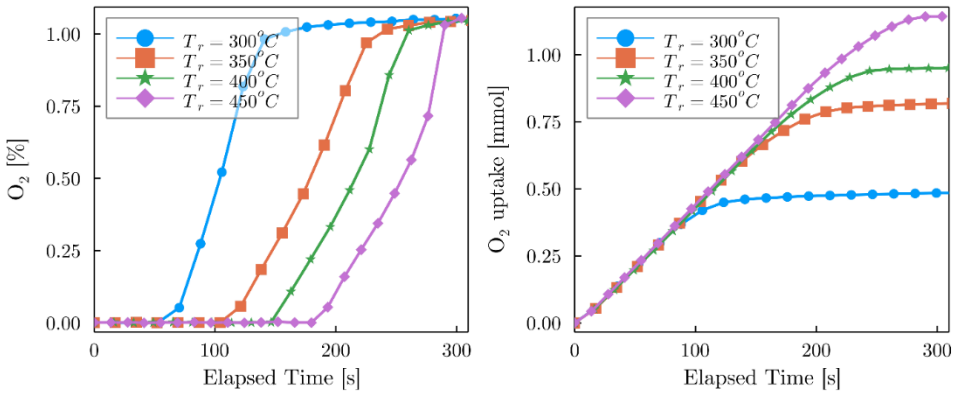

Figure 5. Oxidation of OC with 1% O_2, at different temperatures, left) exit O_2 concentration, right) accumulated O_2 uptake. m_{OC}=0.75g, F_{tot}=600 Nml/min.

4.3 Influence of O_2 concentration on the observed oxidation rate

Higher O_2 concentrations for oxidation of the OC was also tested with 0.75g of OC. Figure 6 shows the results of oxidation of the OC at 450°C with 6% and 20% O_2. Both the first step response with oxidation and the second response without reaction are shown. The O_2-free period was also observed with a higher O_2 concentration, indicating the oxidation kinetic being extremely fast. Actually, if the conversion-time curves with different O_2 concentration are compared, a perfect first order oxidation reaction with respect to O_2 would be concluded. However, as the exit O_2 concentration was zero in the initial fast stage, the inlet O_2 concentration should not be used for the interpretation of oxidation kinetics. It should be noted that, as the oxidation is highly exothermic with a reaction enthalpy of ΔH_r=549.5 [kJ/mol$_{O2}$], a temperature rising was recorded during the oxidation, and the recorded peak was higher with higher O_2 concentration, i.e., more than 50°C with 20% O_2. The temperature rising with higher O_2 concentration also led to a sharper O_2 breakthrough curve because of the fast rate at the higher temperature, as shown in Figure 6b. Kinetically interpretation of the non-isothermal data is generally not possible because of the complicated physical and chemical processes involved [42].

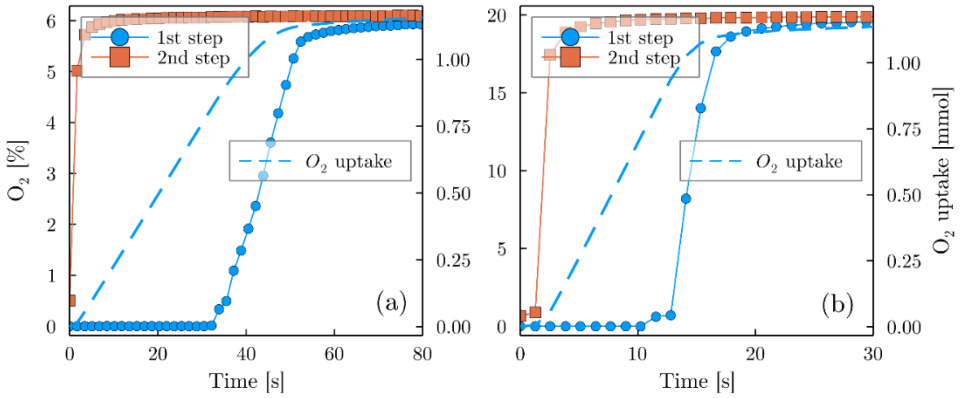

Figure 6. Oxidation of 0.75g OC with different O_2 concentration, (a) 6% O_2, (b) 20% O_2. For both figures, left axis for O_2 concentration at the exit of the fixed bed reactor and right axis for O_2 uptake. F_{tot}=600Nml/min.

4.4 Influence of OC loading on the observed oxidation rate

Lower OC load was tested to confirm the ultra-fast oxidation rate. Figure 7 shows the result of the oxidation 0.15g OC (OC-to-Al_2O_3 mass ratio is about 1:5) at 450°C with 1% O_2. The O_2 concentration was zero in the initial period of the first step response even with such low OC loading, indicating the oxidation being ultra-fast. The O_2 breakthrough came at about 45s. The O_2 breakthrough in the second step response was sharper than that of the first step response, indicating the oxidation rate became slower when the Fe approaching fully converted, which is explained by the oxidation shifted from kinetically-controlled stage to diffusion-controlled stage. Due to the higher dilution ratio and the low O_2 concentration in this test, the temperature rising in this test is below 5°C. Thus, the oxidation rate was estimated using the experimental results with 0.15g OC.

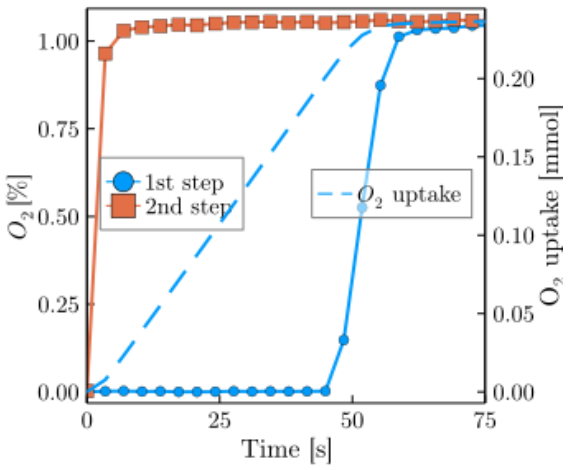

Figure 7. Oxidation of 0.15g OC with ~1.05% O2 in Argon at 450°C, F_{tot} = 600Nml/min.

5 Discussion

As the O_2 concentration was always zero in the initial period of the oxidation, it is not possible to estimate the upper limit of the oxidation rate as a very high oxidation rate also leads to full consumption of O_2. In addition, the information of the variation of oxidation rate with increasing of Fe conversion is largely missing. It is thus not possible to discriminate from different reaction mechanisms. However, the lower limit of the oxidation rate to allow fully consuming O_2 can be estimated, which is achieved by modeling the fixed bed reactor coupling mass transfer and oxidation reaction.

5.1 Estimating the minimum oxidation rate

With the empirical rate equation and n=0-1, Eq.(17), it is determined that the k_r should be at least ~1.3 to allow fully consuming O_2, while the O_2-free time increases with k_r. With k_r = *4.31 [m^3_g/kg_{OC}·s] and n = 0.684,* the simulation of the fixed bed reactor with the 1-D model showed similar exit O_2 concentration curve compared with the experiment at 450°C. Further increase k_r to be greater than 4.31 didn't improve the fit. The phase-boundary controlled reaction (contracting volume) model (n=2/3) was therefore used to simulate the reaction and the comparison between the simulation, and the experimental results of the oxidation with 1% and 20% O_2 is shown in Figure 8. Although the model predicted an earlier O_2 breakthrough, in general, the model fit the experimental results well with a R^2=*0.997*. Therefore, the obtained rate expression:

$$r_{O_2} = 4.31(1 - x_s)^{2/3} C_{O_2}, \qquad \left[\frac{mol_{O_2}}{kg_{OC} \cdot s}\right] \tag{22}$$

is a good estimation of the minimum oxidation rate at 450°C. It is also noted that the O_2 has been fully consumed at 300°C in the initial period, indicating the initial oxidation rate at 300°C should also be in the same magnitude. The rate equation, Eq. (22), is an estimation of the minimum oxidation rate at 450°C. Admittedly, this doesn't mean the mechanism of the oxidation of the OC is phase-boundary controlled. The O_2 concentration was zero before about 45s, the initial local oxidation rate, and the evolution of reaction rate with oxidation conversions are unknown. The oxidation may be much faster in the initial period (e.g., AE0.5 model), or slightly slower in the initial period but increased to the maxima with intermediate conversion (e.g. AEn model with n > 1). It is, however, not possible to be discriminated against those models with the experiments in this work. Moreover, this rate equation doesn't represent the reaction mechanism of the oxidation of Fe as it doesn't predict a dual-peaked TPO curve. Actually, the three-dimensional diffusion grain model, r_{O2}=*4.31/(2*(1-x)$^{1/3}$-1)*, predicts a very similar O_2 exit concentration as the used model. Eq.(22) is only an estimation of minimum oxidation rate.

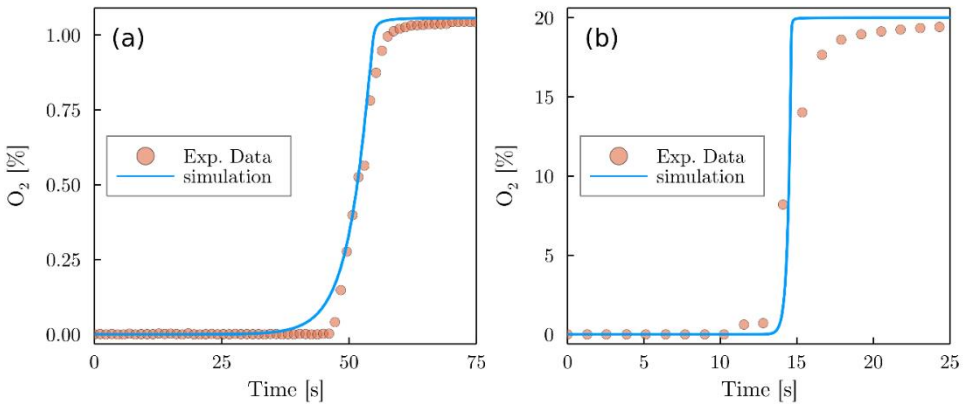

Figure 8. Comparison between the exit O_2 concentration in experiment and simulation. Exp. condition: (a) 0.15g OC, 1.05% O_2 in Ar, (b) 0.75g OC 20% O_2, simulation: k_r = 4.31 [m^3_g/kg_{OC}·s], n = 2/3.

5.2 Transport limitations within the experiment fixed bed

When the reaction is very fast, the interphase and/or intraparticle mass transfer resistance lead to a significant concentration difference between bulk gas and gas on solids or gas concentration gradient inside particles. Therefore, using the gas concentration in the bulk gas to calculate the reaction rate results in significant error. In the tested condition, the superficial gas velocity was about 0.337 [m^3_g/m^2_r·s]. Considering the mixture of 1% O_2 and 99% Argon, the mass transfer coefficient is, k_g=*0.750 [m^3_g/m^2_p·s]*. The maximum mass transfer rate is $k_g a_v C_{O2}/\rho_s$=*1.97 [mol/kg_{OC}·s]* that is about 3 times of the estimated rate (with the bulk O_2 concentration), i.e., $k_r C_{O2}$= *0.762 [mol/kg_{OC}·s]*. Regarding the k_g, Petrovic et al. [52] proposed $\varepsilon j_D = 0.357 \cdot Re_p^{-0.359}$ for low Reynold number flow (*Re>3*). This correlation gives k_g=*0.425 [m^3_g/m^2_p·s]* (with ε=*0.37*), which is in the same magnitude as the one used in the simulation. As the mass transfer rate in the fixed bed reactor for the kinetic test is not significantly greater than the estimated rate, the concentration difference between the bulk gas and gas on the solids is significant. The mass transfer phenomenon was accounted for in the simulation. Figure 9 shows the simulation of the evolution of the Fe conversion, O_2 concentration, and concentration difference between bulk gas and gas on solid in the micro-fixed bed reaction with the estimated minimum oxidation rate. A clear reaction front is seen, indicating the conversion of Fe occurs only in a narrow region of the fixed bed where O_2 is fully consumed, as shown in Figure 9a and b. The concentration difference between the bulk gas and gas on solids surface is about 0.02 [*mol/m^3_g*] that is about 1/6 of the O_2 in bulk gas (e.g., the 3rd spatial point at 5s, C_{O2}=0.12[*mol/m^3_g*], ΔC_{O2}=0.021).

The intraparticle diffusion, which is not modelled in this work, can be quantified using Thiele module. For sphere particles:

$$\phi = R\sqrt{k_r \rho_s / D_{eff}} \tag{23}$$

$$\eta = \frac{3}{\phi^2}(\phi \coth \phi - 1) \tag{24}$$

where ϕ is the Thiele modulus, η is the effectiveness factor, D_{eff} is the effective diffusivity = $\varepsilon_s/\tau(1/D_k+1/D_{Am})^{-1}$ that considers the influence of particle voidage, ε_s, tortuosity, τ, Knudsen diffusion, D_k, and diffusion of A in mixture, D_{Am}. The Knudsen diffusion is calculated by $D_k=1.94(\varepsilon_s/S_g\rho_{Fe2O3})(T/M_w)^{1/2}$, where T is absolute temperature, M_w is the molecular weight of gaseous species [53]. With ε_s=0.5, τ=3, S_g=0.5 [m^2/g], $D_{eff}\approx 9.05\times10^{-6}$ [m^2/s], the effectiveness factor η≈0.684. Thus, the intraparticle diffusion is also significant in the oxidation. Actually, strong intraparticle diffusion limitation indicates that shrinking core model is suitable for describing the gas-solid reaction.

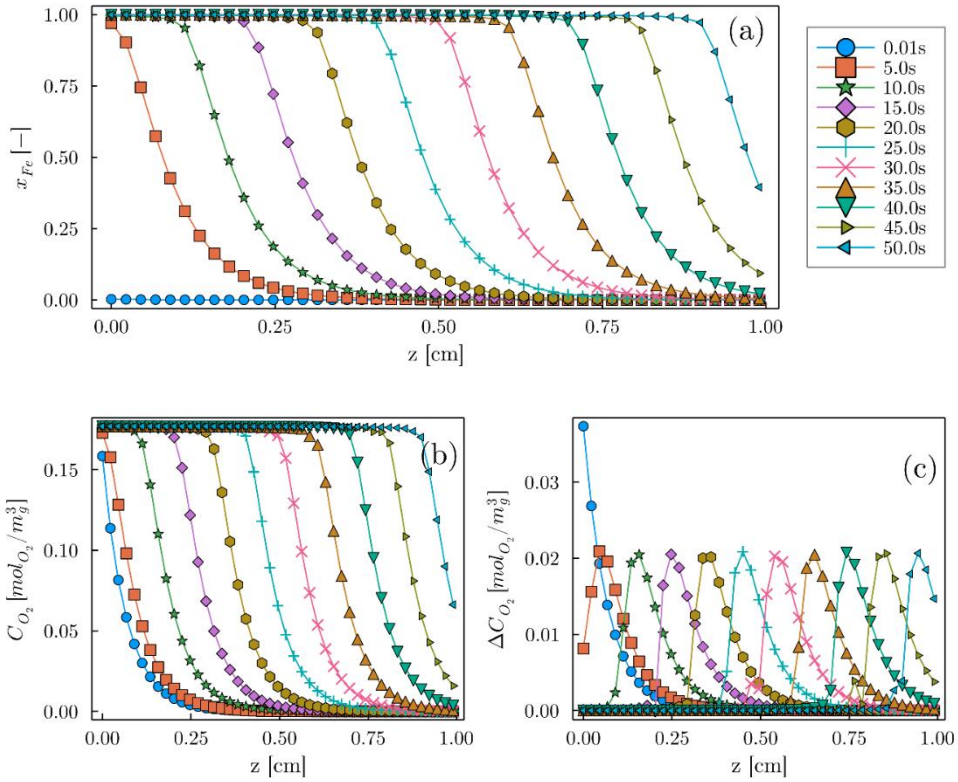

Figure 9. Profile of (a) Fe conversion, (b) O_2 concentration, (c) concentration difference between bulk gas and gas on solids at different time. Simulation, m_{OC}=0.15g, y_{O2}=1%, k_r = 4.31 [$m^3_g/kg_{OC}\cdot s$], n = 2/3.

5.3 Comparison of the oxidation rate with that reported in the literatures

Measuring the oxidation rate of Fe-based OC is changeling because it is extremely fast. The observed oxidation rate is affected largely by the transport phenomena in the experimental setup. As a result, some literature reported very low activation energy that is lower than typical adsorption heat or mass transfer (the apparent activation energy for mass transfer is ~30 kJ/mol [42]). In this work, we determined the minimum rate constant for a ~40s O_2-free period with the shrinking core model. The rate equation in terms of solids conversion is expressed as:

$$\frac{dx_s}{dt} = \frac{1}{C_{Fe}}\frac{4}{3}r_{O_2} = 0.53 \cdot k_r(1-x_s)^{\frac{2}{3}}C_{As}^{s} \quad (25)$$

where C_{Fe}=2.5 [mol_{Fe}/kg_{OC}], k_r>4.31[m^3_g/kg_{OC}·s] at 450°C. For comparison, some reported fast oxidation kinetics are summarized in Table 2 and they are compared with the kinetic estimated in this work. Among the reported oxidation kinetics from ICB-CSIC, the one reported by Cabello et al. [31] is a fast one. Liu et al. [18] used the novel micro-fluidized bed thermogravimetric analysis (MFB-TGA) setup and reported a ~4 times faster rate than that measured in conventional TGA. Although the reported OC was perovskite, the oxidation finished in ~5s that is an ultra-fast one among the literature. It is noted that the fast oxidation kinetics are measured at high temperatures [18,31], while low activation energies were concluded. Thus, extrapolation them to relatively low temperature would not lead to an unrealistically low rate. Buelens [49] investigated the oxidation of Fe by CO_2 using in-situ XRD and reported an activation energy of 108.4 [kJ/mol]. The reaction started from as low as 300°C and could finish below 450°C. Therefore, it is reasonable to compare all oxidation kinetics at 450°C. The solid conversion-time curves of the reported kinetics are compared with the observation in this work in Figure 10. Clearly, the reported minimum oxidation rate in this work is faster than those reported in the literature. It should be noted that Cabello et al. [31] investigated the RedOx system of Fe_2O_3-Fe_3O_4, corresponding to the Fe conversion between 0.88 and 1 in this work. It is noticeable that the oxidation kinetics reported by Buelens et al. [49], using CO_2, is even faster than those using O_2. It seems that the oxidation kinetics measured at high temperature in TGA are questionable.

Table 2. Some reported fast oxidation kinetics.

Oxygen carrier	Rate equation	Reference
Fe_2O_3 on γ-Al_2O_3	$\frac{dx_s}{dt} = 0.346 \cdot \exp\left(-\frac{23{,}000}{RT}\right) C_{O_2}^{0.9}$	Cabello et al. [31]
$CaMn_{0.5}Ti_{0.375}Fe_{0.125}O_{3-\delta}$	$\frac{dx_s}{dt} = 3.8 \cdot \exp\left(-\frac{18{,}770}{RT}\right)(1-x_s)^{\frac{2}{3}}C_{O_2}$	Liu et al. [18]
Fe_2O_3 on $MgAl_2O_4$	$\frac{dx_s}{dt} = 2.39 \cdot 10^7 \exp(-\frac{108{,}400}{RT})(1-x_s)^{\frac{2}{3}}C_{CO_2}$	Buelens et al. [49]

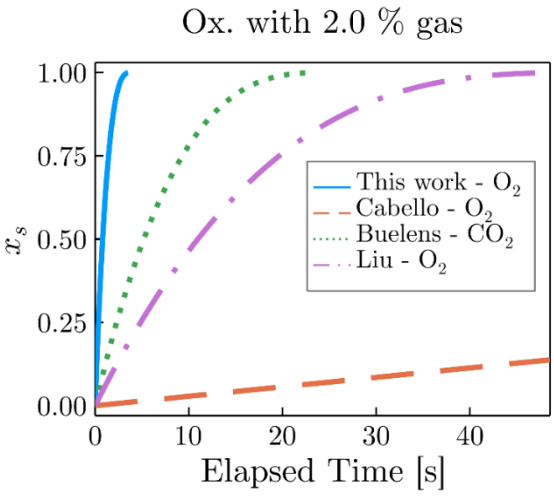

Figure 10. Compare of the oxidation rate and reported kinetics from literature at 450°C with 2% O_2 or CO_2.

5.4 The consequence of the ultra-fast oxidation rate

Because of the ultra-fast rate, the oxidation is generally mass transfer limited in the operating temperature range of chemical looping processes. It is shown in this work, even at a temperature as low as 300°C, accurately measuring the oxidation rate was not achieved. Grosvenor et al. [45] studied the oxidation of Fe at 25-150°C and concluded the activation energy is about 32 [*kJ/mol*]. We suggest to use this activation to extrapolate the oxidation rate as an estimation of the magnitude of the reaction rate at a higher temperature. Because the estimated rate is the minimum rate at 450°C, and the activation energy is relatively low, it is not expected to overestimate the oxidation rate when extrapolating to a high temperature. The rate equation can be then written as:

$$r_{O_2} = 4.31 \exp\left(\frac{32{,}000}{R}\left(\frac{1}{723} - \frac{1}{T}\right)\right)(1 - x_s)^{\frac{2}{3}} C_{O_2}^{S} \tag{26}$$

The interphase mass transfer rate is related to the gas-solid slip velocity. In a bubbling fluidized bed, the diffusivity can be calculated with Sherwood number $Sh=k_g d_p/D_{eff} = 2\varepsilon_{mf}+0.69\cdot Rep^{0.5}Sc^{1/3}$ [54]. The minimum fluidization velocity for the considered OC is 0.019 [$m^3_g/m^2_r \cdot s$] (calculated at 1073K with air, same below). With ε_{mf}=0.5, k_g=*1.21 [m/s]*, and the maximum mass transfer rate is:

$$\frac{k_g a_v}{\rho_s} C_{O2} = 1.21 \times \frac{6}{150 \cdot 10^{-6} \times 2300} \times 2.385 = 42.87 \left[\frac{mol_{O_2}}{kg_{OC} \cdot s}\right] \tag{27}$$

which is lower than the oxidation rate with extrapolation to high 1073K (~58.36 [$mol_{O2}/kg_{OC} \cdot s$] with bulk O_2 concentration). In this case, the oxidation will be completely limited by interphase mass transfer. In addition, the bubbling-emulsion mass transfer is much slower than the gas-solid mass transfer in BFB. The fast oxidation rate leads to the depletion of O_2 in the emulsion phase. Therefore, BFB is not suitable for oxidation even don't consider the hot spot problem. Higher slip velocity can be

achieved in a riser reactor and the maximum slip velocity is the terminal velocity of particles. The terminal velocity of the OC particle (ρ_s=2300 [kg/m^3], d_p = 175μm) is 1.48 m/s. The interphase mass transfer coefficient, k_g, is about 2.671 [$m^3_g/m^2_p \cdot s$]. The initial mass transfer rate, when the surface species concentration is zero, is:

$$k_g \frac{a_v}{\rho_s} C_{O_2} = 2.671 \times \frac{6}{150 \cdot 10^{-6} \times 2300} \times 2.385 = 94.938 \left[\frac{mol_{O_2}}{kg_{OC} \cdot s}\right] \quad (28)$$

That is just slightly higher than the oxidation rate extrapolated from the observed rate (~ 58.361 [$mol_{O2}/kg_{OC} \cdot s$] with bulk O_2 concentration). Thus, mass transfer still plays an important role in the oxidation of the Fe-based OC in the riser.

6 Conclusion

In this work, we reported the experimental study of the oxidation of a newly synthesized Iron-based, $MgAl_2O_4$-supported oxygen carrier (OC). The OC shows a porous structure that facilitates the diffusion of gaseous reactants into the solids. The oxidation of the OC was studied in a micro-fixed bed reactor with a mass spectrometer measuring the effluent gas. Different OC loading (0.75g and 0.15g), O_2 concentration (1%, 6% and 20% with total flow of 600Nml/min) and oxidation temperature (300-450^{o}C) were tested. The Fe-based OC showed an initial fast oxidation period during which the exit O_2 was always zero at all the tested temperature. In every test at 450^{o}C, O_2 was found fully consumed until the OC was nearly fully oxidized, indicating an ultra-fast oxidation rate.

The oxidation rate was evaluated by modeling the fixed bed with a 1-D heterogeneous bed reactor model accounting for the interfacial mass transfer. The empirical gas-solid reaction model was used. Unlike the typical treatment in the literature where the mean concentration of reactant was used while well-mixed solids phase was assumed in kinetics interpretation, the local gaseous reactant concentration and Fe conversion were modeled in evaluating the reaction kinetics. This method enables processing the experimental results with high conversion of gaseous reactant. The estimated minimum rate constant shows that the oxidation rate is very fast that finished within 4s in 2% O_2 at 450^{o}C. The estimated minimum oxidation rate is in the same magnitude of mass transfer in the micro-fixed bed reactor, which also indicates that the intraparticle diffusion played an important role in the oxidation. Extrapolating the reaction rate using relatively low activation energy reported in the literature shows that the oxidation rate is expected to be faster than the mass transfer rate in bubbling fluidized bed and in the same magnitude of mass transfer in the riser.

Acknowledgement

This work is supported by the Fond de la Recherche Scientifique de Belgique (F.R.S.-FNRS) project (T.0230.16). Zirui He acknowledges the financial support from China Scholarships Council (No. 201606220058). The authors would like to thank Dr. Patrick Bussian from Sasol GmbH for providing the MG26 particles, and Prof. Yingjie Li from Shandong University for the valuable advices for revising the manuscript. Computational resources have been provided by the supercomputing facilities of the Université catholique de Louvain (CISM/UCL) and the Consortium des Équipements de Calcul Intensif en Fédération Wallonie Bruxelles (CÉCI) funded by the Fond de la Recherche Scientifique de Belgique (F.R.S.-FNRS) under convention 2.5020.11 and by the Walloon Region.

References

[1] X. Zhu, Q. Imtiaz, F. Donat, C.R. Müller, F. Li, Chemical looping beyond combustion – a perspective, Energy Environ. Sci. 13 (2020) 772–804. https://doi.org/10.1039/C9EE03793D.

[2] D. Li, R. Xu, Z. Gu, X. Zhu, S. Qing, K. Li, Chemical-Looping Conversion of Methane: A Review, Energy Technology 8 (2020) 1900925. https://doi.org/10.1002/ente.201900925.

[3] J. Adanez, A. Abad, F. Garcia-Labiano, P. Gayan, L.F. de Diego, Progress in Chemical-Looping Combustion and Reforming technologies, Progress in Energy and Combustion Science 38 (2012) 215–282. https://doi.org/10.1016/j.pecs.2011.09.001.

[4] A.N. Antzaras, A.A. Lemonidou, Recent advances on materials and processes for intensified production of blue hydrogen, Renewable and Sustainable Energy Reviews 155 (2022) 111917. https://doi.org/10.1016/j.rser.2021.111917.

[5] T. Mendiara, A. Abad, L.F. de Diego, F. García-Labiano, P. Gayán, J. Adánez, Reduction and oxidation kinetics of Tierga iron ore for Chemical Looping Combustion with diverse fuels, Chemical Engineering Journal 359 (2019) 37–46. https://doi.org/10.1016/j.cej.2018.11.022.

[6] J. Chen, F. Donat, L. Duan, A.M. Kierzkowska, S.M. Kim, Y. Xu, E.J. Anthony, C.R. Müller, Metal-oxide stabilized CaO/CuO composites for the integrated Ca/Cu looping process, Chemical Engineering Journal 403 (2021) 126330. https://doi.org/10.1016/j.cej.2020.126330.

[7] Y. Xu, Y. Li, C. Zhang, Y. Wang, J. Zhao, T. Wang, W. Lei, High-Temperature Thermochemical Heat Storage Performance of CaO Honeycombs During CaO/CaCO 3 Cycles, Energy Fuels 35 (2021) 16882–16893. https://doi.org/10.1021/acs.energyfuels.1c02274.

[8] P. Babinski, M. Sciazko, E. Ksepko, Limitation of thermogravimetry for oxy-combustion analysis of coal chars, J Therm Anal Calorim 133 (2018) 713–725. https://doi.org/10.1007/s10973-017-6782-6.

[9] S. Schulze, P. Nikrityuk, Z. Abosteif, S. Guhl, A. Richter, B. Meyer, Heat and mass transfer within thermogravimetric analyser: From simulation to improved estimation of kinetic data for char gasification, Fuel 187 (2017) 338–348. https://doi.org/10.1016/j.fuel.2016.09.048.

[10] W. Hu, F. Donat, S.A. Scott, J.S. Dennis, Kinetics of oxygen uncoupling of a copper based oxygen carrier, Applied Energy 161 (2016) 92–100. https://doi.org/10.1016/j.apenergy.2015.10.006.

[11] T. Mattisson, E. Jerndal, C. Linderholm, A. Lyngfelt, Reactivity of a spray-dried NiO/NiAl2O4 oxygen carrier for chemical-looping combustion, Chemical Engineering Science 66 (2011) 4636–4644. https://doi.org/10.1016/j.ces.2011.06.025.

[12] Z. Zhou, L. Han, G.M. Bollas, Kinetics of NiO reduction by H2 and Ni oxidation at conditions relevant to chemical-looping combustion and reforming, International Journal of Hydrogen Energy 39 (2014) 8535–8556. https://doi.org/10.1016/j.ijhydene.2014.03.161.

[13] M. Su, H. Zhao, X. Tian, P. Zhang, B. Du, Z. Liu, Intrinsic Reduction Kinetics Investigation on a Hematite Oxygen Carrier by CO in Chemical Looping Combustion, Energy Fuels 31 (2017) 3010–3018. https://doi.org/10.1021/acs.energyfuels.6b02827.

[14] C.D. Bohn, J.P. Cleeton, C.R. Müller, J.F. Davidson, A.N. Hayhurst, S.A. Scott, J.S. Dennis, The kinetics of the reduction of iron oxide by carbon monoxide mixed with carbon dioxide, AIChE J. (2010) NA-NA. https://doi.org/10.1002/aic.12084.

[15] W. Liu, J.Y. Lim, M.A. Saucedo, A.N. Hayhurst, S.A. Scott, J.S. Dennis, Kinetics of the reduction of wüstite by hydrogen and carbon monoxide for the chemical looping production of hydrogen, Chemical Engineering Science 120 (2014) 149–166. https://doi.org/10.1016/j.ces.2014.08.010.

[16] H. Chen, Z. Zheng, Z. Chen, X.T. Bi, Reduction of hematite (Fe2O3) to metallic iron (Fe) by CO in a micro fluidized bed reaction analyzer: A multistep kinetics study, Powder Technology 316 (2017) 410–420. https://doi.org/10.1016/j.powtec.2017.02.067.

[17] Z. Qie, H. Alhassawi, F. Sun, J. Gao, G. Zhao, X. Fan, Characteristics and applications of micro fluidized beds (MFBs), Chemical Engineering Journal 428 (2022) 131330. https://doi.org/10.1016/j.cej.2021.131330.

[18] L. Liu, Z. Li, Z. Li, Y. Larring, N. Cai, Heterogeneous reaction kinetics of a perovskite oxygen carrier for chemical looping combustion coupled with oxygen uncoupling, Chemical Engineering Journal 417 (2021) 128054. https://doi.org/10.1016/j.cej.2020.128054.

[19] Y. Li, Z. Li, L. Liu, N. Cai, Measuring the fast oxidation kinetics of a manganese oxygen carrier using microfluidized bed thermogravimetric analysis, Chemical Engineering Journal 385 (2020) 123970. https://doi.org/10.1016/j.cej.2019.123970.

[20] L. Liu, Z. Li, N. Cai, Oxidization and reduction kinetics of a manganese oxygen carrier granulated with the spray drying method at a tonnage scale for chemical looping combustion, Fuel 303 (2021) 121267. https://doi.org/10.1016/j.fuel.2021.121267.

[21] D. Kunii, O. Levenspiel, Fluidization engineering, Elsevier, 1991.
[22] T. Papalas, A.N. Antzaras, A.A. Lemonidou, Intensified steam methane reforming coupled with Ca-Ni looping in a dual fluidized bed reactor system: A conceptual design, Chemical Engineering Journal 382 (2020) 122993. https://doi.org/10.1016/j.cej.2019.122993.
[23] H. Quan, N. Fatah, C. Hu, Diagnosis of hydrodynamic regimes from large to micro-fluidized beds, Chemical Engineering Journal 391 (2020) 123615. https://doi.org/10.1016/j.cej.2019.123615.
[24] Z. He, J. De Wilde, Numerical simulation of commercial scale autothermal chemical looping reforming and bi-reforming for syngas production, Chemical Engineering Journal 417 (2021) 128088. https://doi.org/10.1016/j.cej.2020.128088.
[25] Z. Zhou, G. Deng, L. Li, X. Liu, Z. Sun, L. Duan, Chemical looping co-conversion of CH4 and CO2 using Fe2O3/Al2O3 pellets as both oxygen carrier and catalyst in a fluidized bed reactor, Chemical Engineering Journal 428 (2022) 132133. https://doi.org/10.1016/j.cej.2021.132133.
[26] B. Jin, H. Poelman, C. Detavernier, Z. Liang, G.B. Marin, V.V. Galvita, Microstructured ZrO2 coating of iron oxide for enhanced CO2 conversion, Applied Catalysis B: Environmental 292 (2021) 120194. https://doi.org/10.1016/j.apcatb.2021.120194.
[27] L.C. Buelens, A. van Alboom, H. Poelman, C. Detavernier, G.B. Marin, V.V. Galvita, Fe2O3–MgAl2O4 for CO Production from CO2 Mössbauer Spectroscopy and in Situ X-ray Diffraction, ACS Sustainable Chem. Eng. 7 (2019) 9553–9565. https://doi.org/10.1021/acssuschemeng.9b01036.
[28] J. Hu, H. Li, S. Chen, W. Xiang, Enhanced Fe 2 O 3 /Al 2 O 3 Oxygen Carriers for Chemical Looping Steam Reforming of Methane with Different Mg Ratios, Ind. Eng. Chem. Res. 61 (2022) 1022–1031. https://doi.org/10.1021/acs.iecr.1c03933.
[29] Z. Zhou, L. Li, X. Liu, Z. Zhou, Z. Sun, L. Duan, Accelerated syngas generation from chemical looping CH4 reforming by using reduced ilmenite ore as catalyst, Fuel Processing Technology 232 (2022) 107270. https://doi.org/10.1016/j.fuproc.2022.107270.
[30] A. Abad, J. Adánez, F. García-Labiano, L.F. de Diego, P. Gayán, J. Celaya, Mapping of the range of operational conditions for Cu-, Fe-, and Ni-based oxygen carriers in chemical-looping combustion, Chemical Engineering Science 62 (2007) 533–549. https://doi.org/10.1016/j.ces.2006.09.019.
[31] A. Cabello, A. Abad, F. García-Labiano, P. Gayán, L.F. de Diego, J. Adánez, Kinetic determination of a highly reactive impregnated Fe2O3/Al2O3 oxygen carrier for use in gas-fueled Chemical Looping Combustion, Chemical Engineering Journal 258 (2014) 265–280. https://doi.org/10.1016/j.cej.2014.07.083.
[32] J. Hu, S. Chen, W. Xiang, Sintering and agglomeration of Fe2O3-MgAl2O4 oxygen carriers with different Fe2O3 loadings in chemical looping processes, Fuel 265 (2020) 116983. https://doi.org/10.1016/j.fuel.2019.116983.

[33] R.J. Berger, F. Kapteijn, J.A. Moulijn, G.B. Marin, J. De Wilde, M. Olea, D. Chen, A. Holmen, L. Lietti, E. Tronconi, Y. Schuurman, Dynamic methods for catalytic kinetics, Applied Catalysis A: General 342 (2008) 3–28. https://doi.org/10.1016/j.apcata.2008.03.020.

[34] J. De Wilde, A.K. Das, G.H. Heynderickx, G.B. Marin, Development of a Transient Kinetic Model for the Simultaneous Adsorption of SO2 −NOx over Na/γ-Al2O3 Sorbent, Ind. Eng. Chem. Res. 40 (2001) 119–130. https://doi.org/10.1021/ie000532o.

[35] A.A. Hakeem, M. Li, R.J. Berger, F. Kapteijn, M. Makkee, Kinetics of the high temperature water–gas shift over Fe2O3/ZrO2, Rh/ZrO2 and Rh/Fe2O3/ZrO2, Chemical Engineering Journal 263 (2015) 427–434. https://doi.org/10.1016/j.cej.2014.10.104.

[36] F. Minette, M. Lugo-Pimentel, D. Modroukas, A.W. Davis, R. Gill, M.J. Castaldi, J. De Wilde, Intrinsic kinetics of steam methane reforming on a thin, nanostructured and adherent Ni coating, Applied Catalysis B: Environmental 238 (2018) 184–197. https://doi.org/10.1016/j.apcatb.2018.07.015.

[37] A. Scaltsoyiannes, A. Lemonidou, CaCO3 decomposition for calcium-looping applications: Kinetic modeling in a fixed-bed reactor, Chemical Engineering Science: X 8 (2020) 100071. https://doi.org/10.1016/j.cesx.2020.100071.

[38] A. Scaltsoyiannes, A. Antzaras, G. Koilaridis, A. Lemonidou, Towards a generalized carbonation kinetic model for CaO-based materials using a modified random pore model, Chemical Engineering Journal 407 (2021) 127207. https://doi.org/10.1016/j.cej.2020.127207.

[39] W. Liu, M. Ismail, M.T. Dunstan, W. Hu, Z. Zhang, P.S. Fennell, S.A. Scott, J.S. Dennis, Inhibiting the interaction between FeO and Al2O3 during chemical looping production of hydrogen, RSC Adv. 5 (2014) 1759–1771. https://doi.org/10.1039/C4RA11891J.

[40] A. Longo, S.A. Theofanidis, C. Cavallari, N.V. Srinath, J. Hu, H. Poelman, M.K. Sabbe, C.J. Sahle, G.B. Marin, V.V. Galvita, What Makes Fe-Modified MgAl2O4 an Active Catalyst Support? Insight from X-ray Raman Scattering, ACS Catal. 10 (2020) 6613–6622. https://doi.org/10.1021/acscatal.0c00759.

[41] V. Singh, L.C. Buelens, H. Poelman, M. Saeys, G.B. Marin, V.V. Galvita, Carbon monoxide production using a steel mill gas in a combined chemical looping process, Journal of Energy Chemistry 68 (2022) 811–825. https://doi.org/10.1016/j.jechem.2021.12.042.

[42] G.F. Froment, J. De Wilde, K.B. Bischoff, Chemical Reactor Analysis and Design, Third Edition, Wiley, Hoboken, N.J., 2010.

[43] E.N. Fuller, P.D. Schettler, J.C. Giddings, New method for prediction of binary gas-phase diffusion coefficients, Industrial & Engineering Chemistry 58 (1966) 18–27.

[44] A.P. Grosvenor, B.A. Kobe, N.S. McIntyre, Examination of the oxidation of iron by oxygen using X-ray photoelectron spectroscopy and QUASESTM, Surface Science 565 (2004) 151–162. https://doi.org/10.1016/j.susc.2004.06.210.

[45] A.P. Grosvenor, B.A. Kobe, N.S. McIntyre, Activation energies for the oxidation of iron by oxygen gas and water vapour, Surface Science 574 (2005) 317–321. https://doi.org/10.1016/j.susc.2004.10.043.

[46] J. Bezanson, A. Edelman, S. Karpinski, V.B. Shah, Julia: A Fresh Approach to Numerical Computing, SIAM Rev. 59 (2017) 65–98. https://doi.org/10.1137/141000671.

[47] C. Rackauckas, Q. Nie, 2017. DifferentialEquations.jl – A Performant and Feature-Rich Ecosystem for Solving Differential Equations in Julia. Journal of Open Research Software 5, 15. https://doi.org/10.5334/jors.151.

[48] C.A. Kennedy, M.H. Carpenter, Higher-order additive Runge–Kutta schemes for ordinary differential equations, Applied Numerical Mathematics 136 (2019) 183–205. https://doi.org/10.1016/j.apnum.2018.10.007.

[49] L.C. Buelens, V.V. Galvita, H. Poelman, C. Detavernier, G.B. Marin, Kinetics of Multi-Step Redox Processes by Time-Resolved In Situ X-ray Diffraction, Chemie Ingenieur Technik 88 (2016) 1684–1692. https://doi.org/10.1002/cite.201600057.

[50] Z. Li, General rate equation theory for gas–solid reaction kinetics and its application to CaO carbonation, Chemical Engineering Science 227 (2020) 115902. https://doi.org/10.1016/j.ces.2020.115902.

[51] Z. Zhao, M. Uddi, A.F. Ghoniem, Redox kinetics of nickel oxide foils: Structural evolution and rate-limiting steps, Combustion and Flame 207 (2019) 71–88. https://doi.org/10.1016/j.combustflame.2019.05.012.

[52] L.J. Petrovic, G. Thodos, Mass Transfer in Flow of Gases through Packed Beds. Low Reynolds Number Region, Ind. Eng. Chem. Fund. 7 (1968) 274–280. https://doi.org/10.1021/i160026a016.

[53] C.N. Satterfield, Heterogeneous Catalysis in Industrial Practice, McGraw-Hill Company, 1981.

[54] J.S. Dennis, A.N. Hayhurst, A simplified analytical model for the rate of reaction of SO2 with limestone particles, Chemical Engineering Science 41 (1986) 25–36. https://doi.org/10.1016/0009-2509(86)85194-6.